

Lab on a Chip

Accepted Manuscript



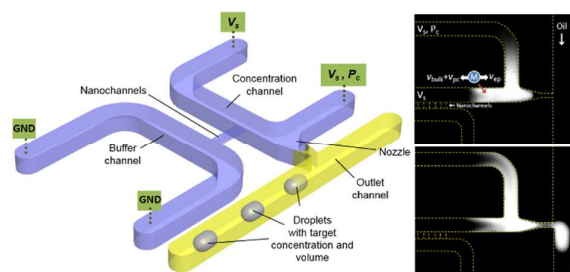
This is an *Accepted Manuscript*, which has been through the Royal Society of Chemistry peer review process and has been accepted for publication.

Accepted Manuscripts are published online shortly after acceptance, before technical editing, formatting and proof reading. Using this free service, authors can make their results available to the community, in citable form, before we publish the edited article. We will replace this *Accepted Manuscript* with the edited and formatted *Advance Article* as soon as it is available.

You can find more information about *Accepted Manuscripts* in the [Information for Authors](#).

Please note that technical editing may introduce minor changes to the text and/or graphics, which may alter content. The journal's standard [Terms & Conditions](#) and the [Ethical guidelines](#) still apply. In no event shall the Royal Society of Chemistry be held responsible for any errors or omissions in this *Accepted Manuscript* or any consequences arising from the use of any information it contains.

We developed an on-demand nanofluidic concentrator that can adaptively encapsulate highly concentrated samples and enhance long-term stability for further analysis.



ARTICLE

An on-demand nanofluidic concentrator

Cite this: DOI: 10.1039/x0xx00000x

Miao Yu,^a Youmin Hou,^b Hongbo Zhou,^{b,c} and Shuhuai Yao^{*a,b}

Received 00th January 2015,

Accepted 00th January 2015

DOI: 10.1039/x0xx00000x

www.rsc.org/

Preconcentration of biomolecules by electrokinetic trapping at the nano/microfluidic interface has been extensively studied due to its significant concentration efficiency. Conventionally, the sample preconcentration takes place in continuous flow and therefore suffers from diffusion and dispersion. Encapsulation of the preconcentrated sample into isolated droplets offers a superior way to preserve sample concentration for further analysis. Nevertheless, the rationale for an optimal design to obviate the sample dilution prior to encapsulation is still lacking. Herein, we proposed an assisting pressure strategy for positioning the concentrated sample plug directly at the ejecting nozzle, which greatly eliminates the concentration decline during sample ejection. Distinctive mechanism of such plug localization was elucidated by two-dimensional numerical simulations. Based on the simulation results, we developed an on-demand nanofluidic concentrator in which the nanochannels were facilely generated through lithography-free nanocracking on polystyrene substrate. By wisely implementing an on-demand droplet generation module, our system can adaptively encapsulate the highly concentrated sample and effectively enhance the long-term stability. We experimentally demonstrated a preconcentration of a fluorescence labelled biomolecule, bovine serum albumin (BSA), by an amplification factor of 10^4 . We showed that, by adjusting the applied voltage, accumulation time, and pulsed pressure imposed on the control microchannel, our system can generate a droplet of desired volume with a target sample concentration at a prescribed time. This study not only provides insights into the previously unidentified role of assisting pressure on sample positioning, but also offers an avenue for varied requirements in low-abundant biomolecule detection and analysis.

Introduction

Biomarkers are measurable characteristics that indicate not only normal biological processes, but also disease types, stages, and pharmacologic responses to therapies.¹ Biomarker assays are thus invaluable tools for disease detection, diagnosis and treatment selection. The widely investigated biomarkers for disease detection and prediction include nucleic acids, proteins and metabolites.² Yet, due to the low-abundance of biomarkers in the biofluids, sample preconcentration is often required to increase the biomolecule concentration above the detection limit for bioassays.³ Over the past few decades, sample preconcentration techniques including capillary electrophoresis⁴, field-amplified sample stacking⁵, isotachopheresis⁶, bipolar electrode focusing⁷, and ion concentration polarization (ICP)⁸⁻¹⁰ have been developed. The most efficient biomolecule concentrator based on ICP that utilizes electrokinetic trapping at the nano/microchannel junction has achieved local concentration enrichment up to a million-fold.¹¹ Ions and charged molecules, regardless of their sizes or types, can be efficiently concentrated at both the cathodic and anodic sides of the nanochannels or nanomembranes.¹²⁻¹⁷

The commonly used sample preconcentration by ICP occurs in continuous flow, where the concentrated sample plug is susceptible to diffusion and dispersion. Without the maintenance of electric fields or the assistance of valves¹⁴, the concentrated

sample plug will be rapidly diluted¹⁸ prior to any further detection or reaction. A better way of sample handling is to encapsulate the concentrated sample into water-in-oil droplets that can be further manipulated and detected on-chip or off-chip. In contrast to the continuous flow, the discrete droplets restrict the diffusion in confined spaces and are relatively easy for manipulation,¹⁹⁻²¹ thereby facilitating long-time, multi-step detections or a series of simultaneous reactions. As demonstrated by Chen et al.²², an integrated device that consisted of a biomolecule concentrator and a microdroplet generator was applied to multiplexed enzyme assays, which allowed for significant reduction in the reaction time and sample volume used. However, the trapping zone induced by ICP was far away from the ejection nozzle, and the applied voltage had to be turned off when the preconcentrated plug was translocated. Therefore, sample dilution and dispersion were still inevitable before the droplet ejection. Moreover, the concentration and volume of the generated droplets cannot be adaptively controlled to meet the different requirements of further detection or reaction.

To overcome these limitations, here we developed an ingenious on-demand droplet-based nanofluidic concentrator consisting of a hybrid polystyrene-PDMS nano/microchannel network. The nanochannels were conveniently formed by lithography-free nanocracking on a polystyrene (PS) substrate and bonded with PDMS microchannels replica. To prevent the propagation of the concentration polarization and localize the enriched sample plug at a target position in a dual

nano/microchannel system, we adopted an additional hydrodynamic pressure on the network and studied its working principle for sample molecule trapping and positioning in two-dimensional simulations. After that, we carried out experiments using FITC-BSA as the sample and demonstrated that the highly concentrated plug could be positioned at the ejection nozzle for droplet encapsulation, with the help of DC voltage and pressure difference across the inlets. By adjusting the applied voltage and pressure, the formed nanoliter droplets can be controlled simultaneously in concentration, volume, and formation time.

Experimental

System design

The proposed system consists of a nanofluidic concentrator and a droplet-on-demand (DOD) generator previously demonstrated

by our group.^{23, 24} As illustrated in Figure 1(a), the DOD system is based on a T-junction microchannel for droplet formation, which includes a carrier phase of mineral oil and a discrete phase of samples in aqueous solution. To facilitate the on-demand control for droplet formation, in our system, a nozzle (a narrower channel) is introduced at the T-junction to form a Laplace pressure barrier P_{barrier} between the two immiscible phases, keeping the interface at the nozzle.²⁵ The nanofluidic concentrator is based on two microchannels bridged by nanochannels. One microchannel is filled with the buffer solution and connected to the ground potential. The other microchannel is filled with the sample solution and connected to the applied voltage ($V_s > 0$). The sample channel is further divided into two parts by the nozzle, resulting in a concentration channel that is directly connected to the nanochannels, and a control channel that is used for positioning the enriched sample plug to the desired location.

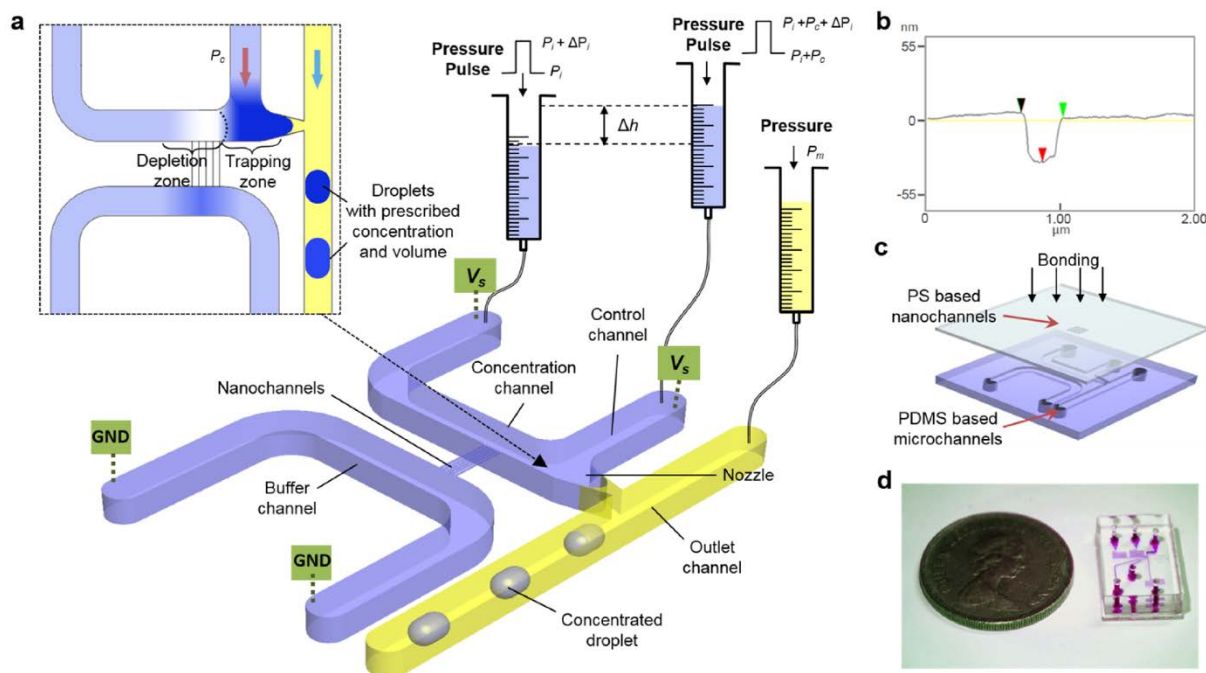


Figure 1. (a) Schematic diagram of the nanofluidic concentrator coupled with a droplet-on-demand system. The sample is accumulated and positioned near the nozzle by tuning the applied voltage V_s and assisting pressure P_c . Then a pressure pulse ΔP_i is imposed on the sample channel and the concentrated plug is encapsulated into a water-in-oil droplet. By adjusting the applied voltage, accumulation time, and pulsed pressure, a droplet with desired concentration and volume can be generated at a prescribed time. (b) AFM image of a nanochannel (33 nm deep and 309 nm wide) developed on a PS substrate. (c) Schematic showing the bonding process of PS nanochannels with PDMS microchannels. (d) Optical image of the device.

When a positive electric potential (V_s) is applied across the sample and buffer channels, due to the electrical double layer (EDL) formed in the nanochannels, the unequal migrations of the co-ions and counter-ions in the buffer solution result in an ion depletion zone near the interface between the sample channel and the nanochannels. Near the interface, the target molecules in the sample channel can be continuously trapped. A pressure difference (P_c), generated by adjusting the height of the reservoirs between the control and concentration channels (refer to Fig.S2†), is used to stabilize and position the enriched sample plug near the nozzle. After the enriched sample reaches a desired concentration, a pulsed pressure ΔP_i imposed on the sample channel will break the pressure barrier at the nozzle, encapsulating the sample plug into a water-in-oil droplet. By tuning the applied voltage, accumulation time, pulse amplitude

and pulse duration, a droplet with a target concentration and volume can be generated at a prescribed time.

Chemicals and apparatus

The sample molecule used in this work is bovine serum albumin (BSA), labelled with FITC (Sigma-Aldrich). The background electrolyte, phosphate buffered saline (PBS), was prepared using sodium phosphate, sodium chloride (Sigma-Aldrich) and Milli-Q deionized water (Millipore). Prior to each experiment, the sample and buffer were freshly prepared from stock solutions. Mineral oil (0.84 g/mL at 25 °C, Sigma-Aldrich) was used for water-in-oil emulsion.

For fabrication, PS Petri dishes (60 mm × 15 mm) were obtained from SPL Life Sciences, and Sylgard 184 PDMS kit was obtained from Dow Corning Inc. Surface treatment

chemicals including hexadecane, trichloro (1H,1H,2H,2H-perfluorooctyl) silane, trichloro (octadecyl) silane (OTS), and 3-aminopropyltriethoxysilane (APTES) were obtained from Sigma-Aldrich.

An inverted microscope (Eclipse Ti-U, Nikon) coupled with a CCD camera (The EXi Blue, QImaging) was used for imaging. A LED light source (490 nm, Thorlabs) was guided to the microscope via a collimation adapter. An FITC filter cube (excitation: 465-495 nm, dichroic mirror: 505 nm, emission: 515-555 nm, Nikon) was used. To determine the sample concentration, a calibration of fluorescence intensity with different FITC-BSA concentrations was carried out (refer to Fig.S3†).

A Keithley 6487 picoammeter/voltage source with platinum probes (Omega) was used to supply the electric potential and measure the electric current. For the pressure control, a home-made LabVIEW-controlled air pressure regulator was used.

Device fabrication

The microchannels were produced following a general PDMS chip fabrication process. First, the master of PDMS microchannels was developed on a silicon wafer by standard photolithography (SUSS Microtec MA6) and deep reactive ion etching (DRIE, STS ICP DRIE Silicon Etcher). The resulting microchannels were 50 μm deep. The sample channel and buffer channel were 50 μm wide, and the nozzle was 25 μm wide. To help release the PDMS replica from the master, the silicon wafer was treated with trichloro(1H,1H,2H,2H-perfluorooctyl) silane and put in a vacuum chamber for one hour. Then, PDMS base and curing agent were mixed in a ratio of 10:1 by weight. The mixture was poured onto the master after degassing for 30 minutes. After curing the mixture in a 65 $^{\circ}\text{C}$ oven for 4 hours, the cured PDMS was peeled off from the wafer and cut into small pieces of chips with a blade. Holes were punched using a pan needle.

For the fabrication of the nanochannel array, we employed a lithography-free approach of large-scale nanocracking generated on a PS surface developed by Xu et al²⁶. Detailed fabrication procedure can be found in Fig. S1†. The PS surface experienced an initial swell caused by the interaction with hot ethanol vapour, and then a sudden shrink due to the complete release of ethanol, resulting in nanoslits that were 32 ± 4 nm deep and 310 ± 24 nm wide, as shown in Figure 1(b).

The fabricated PDMS microchannel replica and the nanocracked PS substrate were aligned for bonding (Figure 1(c)). To make sufficiently strong bonding between the PS thermoplastic and PDMS (e.g., pressure is 20 kPa maximum in this work), we employed a strong and irreversible bonding technique at room temperature.²⁷ The PS surface was soaked in 5% v/v APTES water solution and placed on a hot plate at 80 $^{\circ}\text{C}$ for 20 min, and then cleaned with DI water and dried with nitrogen gas. The PDMS replica and PS surface were treated with O₂ plasma for 60 sec and 10 sec, respectively. After aligning the PDMS microchannels with the nanoslits in the PS substrate, a heavy block was placed on the chip for one hour to enhance the bonding. For generating aqueous droplets in oil, OTS solution in hexadecane (1%, v/v) was carefully introduced into the outlet channel for 2 min and then flushed out with pure hexadecane. The resulting OTS coating ensured the hydrophobicity of the microchannel surface for the oil phase, so that the droplets generated at the nozzle maintained high reproducibility.

Numerical modelling

To elucidate the mechanism of sample preconcentration near the nano/microchannel junction and concentrated plug positioning via assisting pressure, we carried out simulations based on a simplified two-dimensional nano/microfluidic hybrid system, as shown in Figure 2(a). The total flux J_i of ion/molecule i is given by the extended Nernst-Planck equation²⁸,

$$J_i = -D_i \nabla c_i - \frac{z_i F}{RT} D_i c_i \nabla \phi + c_i \bar{u} \quad (1)$$

where D_i , c_i , z_i are the diffusion coefficient, concentration, and valence of ion/molecule i ($i = 1$ and 2 for potassium and chloride ions of the background buffer, and $i = 3$ for BSA molecules), F is the Faraday constant, R is the gas constant, T is the absolute temperature, ϕ is the electric potential, and \bar{u} is the velocity vector of the bulk flow. The concentration of KCl solution at four reservoirs is set as 10 mM. The concentration of BSA molecules at the sample channel ends is 10 nM while at the buffer channel ends is 0. The valence of BSA is set as -2.²⁹ For the diffusion coefficient, $D_1 = 1.96 \times 10^{-9}$ m²/s, $D_2 = 2.03 \times 10^{-9}$ m²/s, and $D_3 = 3 \times 10^{-10}$ m²/s.³⁰

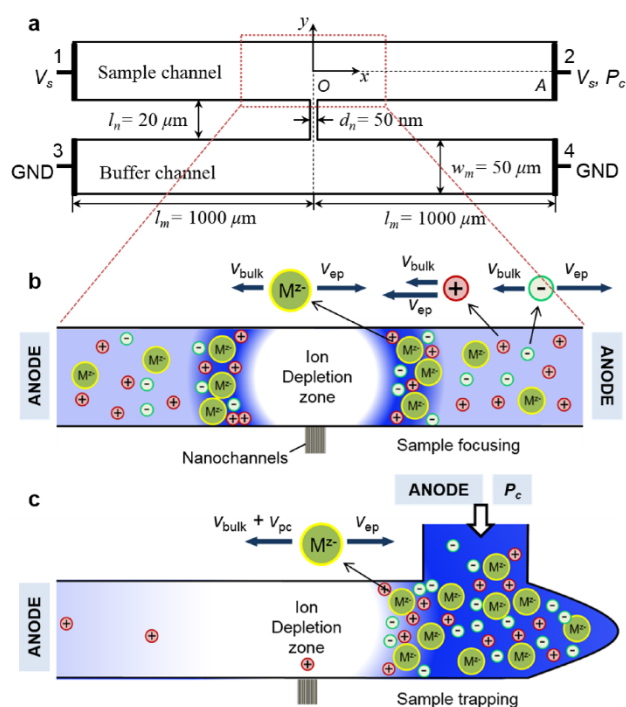


Figure 2. (a) Schematic drawing of a 2D hybrid nano/microfluidic fluidic system used in numerical simulations (not drawn to scale). Schematics showing (b) the mechanism of ion concentration polarization and biomolecule preconcentration in an anodic microchannel near the junction of nano/microchannels, and (c) stabilizing and positioning the trapping plug near the nozzle with an assisting pressure P_c .

For each particle, mass conservation requires,

$$\frac{\partial c_i}{\partial t} = -\nabla \cdot J_i \quad (2)$$

The Poisson equation describes the electric potential distribution,³¹

$$\nabla^2 \phi = -\frac{F}{\epsilon_0 \epsilon_r} \sum_{i=1}^3 z_i c_i \quad (3)$$

where ϵ_0 is the permittivity of vacuum. The relative permittivity ϵ_r is 80. Boundary condition for the electric potential on the channel walls is given by,

$$\nabla_{\perp} \phi = -\frac{\sigma}{\epsilon_0 \epsilon_r} \quad (4)$$

where \perp denotes the wall-normal component, and σ is the surface charge density of the channel walls. The surface charge density is assumed to be uniformly at -5 mC/m^2 .

For incompressible laminar flow, by neglecting the inertia term³², the velocity distribution can be solved by the Navier-Stokes equations,

$$-\nabla p + \eta \nabla^2 \bar{u} - F \sum_{i=1}^3 z_i c_i \nabla \phi = 0 \quad (5)$$

$$\nabla \cdot \bar{u} = 0 \quad (6)$$

where p is the hydrostatic pressure and η is the fluid viscosity. Nonslip boundary conditions are assumed on the channel walls for the fluid velocities. The coupled Nernst-Planck equations, Poisson equation, and Navier-Stokes equations are solved using a finite element analysis software package Comsol Multiphysics. For the initial conditions, we firstly set both external pressure and voltage supply as zero, and solved the model using the stationary solver. The results were used as the initial conditions for the following time-dependent calculation. To ensure the finite difference algorithm convergence, the external pressure and voltage supply were smoothed by the Heaviside step function changing from zero to P_c and V_s respectively with the time duration of 10^{-5} s .^{13, 29}

Results and discussion

Mechanism of ion concentration polarization

As illustrated in Figure 2(b), the motions of ions/charged molecules in the nano/microfluidic network are mainly determined by the electrophoretic velocity and the bulk flow velocity.³³ The bulk flow results from a combined effect of the electroosmotic flow and the induced internal pressure gradient^{34, 35}. For ions such as K^+ and Cl^- with higher electrophoretic mobility, their motions are dominated by the electrophoretic velocity. For negatively charged molecules like BSA at moderate ionic strength here, the electrophoretic and electroosmotic contributions are comparable, but in the opposite directions.³⁶

Applying an electrical potential difference of V_s across the sample and buffer channels as shown in Figure 2(a), the cations K^+ migrate from the sample channel to the buffer channel through the nanochannel while the anions Cl^- are constrained from migrating to the sample channel because of the formation of the EDLs on the nanochannel surface. As a result, the anions are depleted at the junction. To maintain the electroneutrality, cations are depleted in a similar manner as the anions. Therefore, an ionic depletion zone is created at the junction as shown in Figure 2(b). The resulted conductivity gradient establishes a sharp electric field gradient near the junction. The electrophoretic force, which drives the negatively charged molecules to transport from the region of lower to higher electric field, is countered by a constant bulk flow. Since the local electrophoretic velocity is proportional to the corresponding electric field, the molecules decelerate and stack as they move along the electric field gradient, which results in a concentration enrichment phenomenon called gradient focusing³⁷. Figure 3(a) presents the simulation results of BSA concentration profile in the sample channel at $t = 20 \text{ s}$, 40 s and 60 s when $V_s = 20 \text{ V}$. In this condition, the concentration peak of the negatively charged BSA molecules keeps migrating away from the nano/microchannel junction, because the bulk flow velocity cannot match the electrophoretic velocity. Though the concentration of the enriched peak increases at first, the

concentrated plug becomes broaden during the migration, and finally the peak concentration flattens out due to the diffusion when the plug shifts far away from the nanochannel, where the conductivity gradient becomes negligible. This unstable preconcentration process cannot meet our requirements for on-demand encapsulation of the enriched sample, so a strategy for stabilizing and positioning the concentrated sample plug is needed.

The preconcentrated sample plug positioning

An additional flow induced by external pressure or voltage bias has been demonstrated for strengthening the bulk flow and balancing the electrophoretic flow so that a focal point can be found where the transport velocity of target molecules becomes zero and the molecules are trapped locally.^{29, 36, 38} Here we took the strategy of applying a hydrodynamic assisting pressure P_c at the reservoir of the control channel (Figure 2(c)) to tune and stabilize the location of the concentrated sample plug.

To elucidate the mechanism of positioning the concentrated plug at a specific location with an assisting pressure, we simulated the concentration process with P_c applied on reservoir 2 in Figure 2(a). Since the transport of BSA molecule is mainly governed by the competition between the electrophoretic and bulk flow velocities, by neglecting the diffusion effect, we first studied the net transport velocity variation as a function of the assisting pressure. Electric potential $V_s = 20 \text{ V}$ and different pressure P_c ranging from 0 to 0.7 Pa were applied to the network. Figure 3(b) presents the net velocity profiles of BSA molecule along the centerline OA as indicated in Figure 2(a). When no pressure is applied, the velocity is above the zero velocity axis, and thus the concentrated plug keeps migrating to the reservoir as Figure 3(a) shows. When $P_c = 0.5 \text{ Pa}$ is applied, the velocity profile intersects with the zero velocity axis at two equilibrium points. The intersection with the negative derivative (as circled in Figure 3(b)) is termed as the focal point, where the net velocity is zero and the molecules are locally stacked. By increasing P_c , the velocity profile moves downward and the focal point shifts towards the nanochannel. Therefore, by tuning the assisting pressure, the sample molecules will be trapped at different locations along the microchannel. However, if P_c is so high that the velocity profile of BSA cannot intersect with zero velocity axis, the concentration process would be hindered.

Figure 3(c) shows the movement of the concentration peak along the centerline OA over time at $V_s = 20 \text{ V}$ and $P_c = 0.45, 0.5$ and 0.55 Pa . At the beginning, when the voltage and assisting pressure are applied to the network, the initial bulk flow velocity for BSA molecules in the microchannel is greater than its electrophoretic velocity. Hence, the molecules first transport from the reservoir to the nano/microchannel junction, and stack at the entrance of the nanochannel due to the strong EDL exclusion inside. As the ion concentration near the junction further depletes, the bulk flow velocity and electrophoretic velocity of BSA both increase with the rising electric field, but the bulk flow increases more slowly because of the overlapped EDL formed in the nanochannel. Specifically, when the EDL in the nanochannel overlaps, the electroosmotic velocity in the nanochannel is weakened from $\mu_{eo} E_x$ to $\mu_{eo} E_x (1 - \psi/\zeta)$, where μ_{eo} is the electroosmotic mobility, E_x is the electric field in x direction, ψ is the potential distribution and ζ is the zeta potential.³² As a result, the electroosmotic flow rate in the nanochannel is lower than the microchannel. To maintain the balance between the bulk flow rates in the nanochannel and microchannel, an induced pressure is generated near the junction to form an internal flow and suppress the ever-growing

electroosmotic flow in the microchannel. Therefore, the restrained bulk flow velocity in the microchannel cannot increase as fast as the electrophoretic velocity for BSA molecules. As the local electrophoretic velocity near the junction surpasses the bulk flow velocity in the microchannel, the concentrated plug starts to shift towards the reservoir at a gradually diminished moving speed and finally becomes stationary when the ionic polarization process reaches the equilibrium status. Figure 3(d) demonstrates the concentration distribution of BSA molecules within the

microchannel at $V_s = 20$ V and $P_c = 0.52$ Pa. The concentration peak is held at ~ 90 μm from the junction. Note that, under the same condition of V_s and P_c , the actual concentration peak is located further from the nanochannel than the focal point analyzed in Figure 3(b). This is because the diffusion effect was not taken into account for the focal point analysis, while the diffusive velocity would push the concentration peak towards the reservoir.

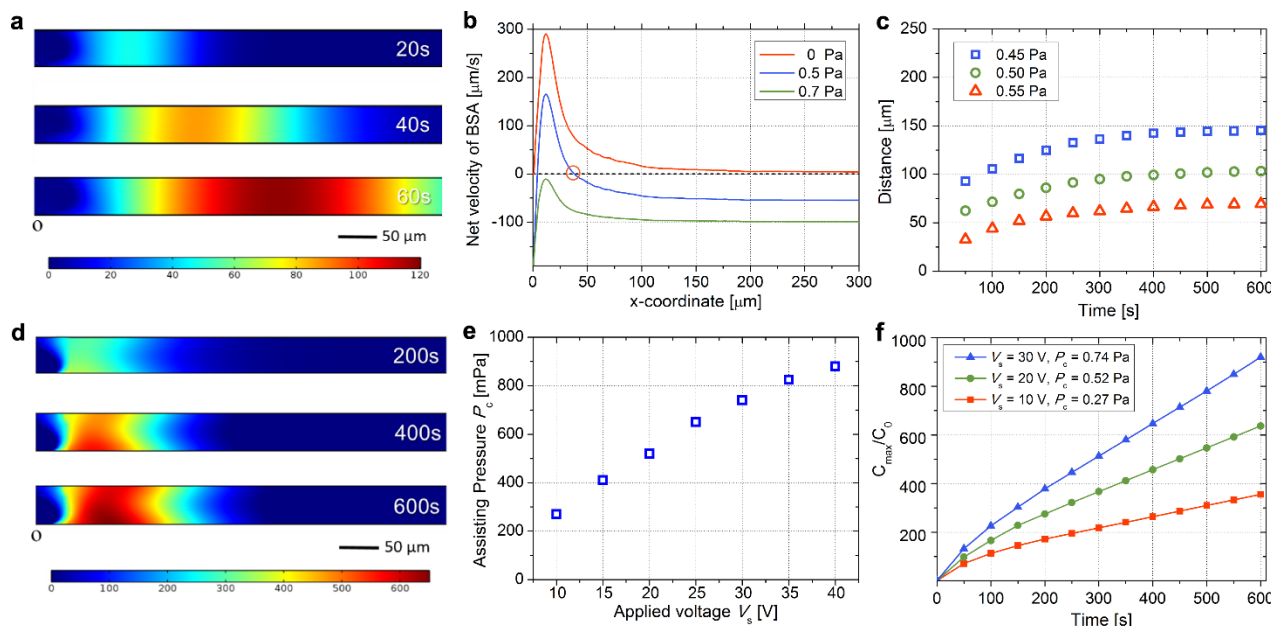


Figure 3. (a) Simulation results of the BSA concentration distribution in the sample channel (only the right half of the channel is shown). The applied voltage V_s is 20 V. (b) Net velocity of BSA along the centerline OA of the channel at $V_s = 20$ V and different assisting pressure P_c . (c) Influence of the assisting pressure P_c on the displacement of the concentration peak along the centerline OA at $V_s = 20$ V. (d) The BSA concentration distribution in the sample channel at $V_s = 20$ V and $P_c = 0.52$ Pa. (e) The relationship between V_s and P_c for positioning the concentration peak at a distance of 90 μm from the nanochannel. (f). Evolution of the peak concentration for various combinations of V_s and P_c .

To locate the sample plug at a prescribed position, the relationship between V_s and P_c was also studied. For a given V_s , we adjusted P_c so that the concentration peak was kept at ~ 90 μm from the junction. As shown in Figure 3(e), P_c initially varies almost linearly with V_s , while subsequently grows more gradually when V_s becomes high. This is because, under low voltage supply, when V_s is doubled, the electrophoretic velocity of BSA is doubled. So the velocity induced by the assisting pressure also needs to be doubled to keep the balance. Yet, when applied voltage is high, under moderate (e.g. 10 mM buffer as used here) or high background ionic strength, the electrophoretic flow tends to saturate due to the polarization effect.³⁹ Therefore, as V_s is enhanced, P_c increases nonlinearly. Figure 3(f) gives the evolution of peak concentration along the centerline OA of the sample channel for different combinations of V_s and P_c under which the peaks are kept at the same position. The peak concentration increases almost linearly with time, which is suitable for the purpose of controllable pre-concentration.

Protein enrichment by the nanofluidic concentrator

Based on the control scheme studied in the simulations, we designed our PDMS-PS nanoconcentrator chip as shown in Figure 1(d). The assisting pressure P_c was generated by adjusting the relative heights of the reservoirs between the control and concentration channels. To demonstrate the performance of the droplet-based concentrator, we used FITC-

BSA to measure the pre-concentration factor under various experimental conditions. Before each measurement, the device was thoroughly flushed by 0.1 M NaOH for 2 min and PBS buffer for 5 min successively to ensure the same initial condition. The sample microchannel was initially filled with 10 nM FITC-BSA in 0.1X PBS solution (~ 10 mM, pH = 7.4). Pressures P_i and P_m were adjusted as 13.6 kPa and 12.8 kPa, respectively, to keep the immiscible phase interface at the nozzle. Different electric potentials were tested to demonstrate the on-demand controllability of the concentrator.

As shown in Figure 4(a), when $V_s = 120$ V and $P_c = 1.52$ kPa were applied between the concentration and buffer channels, the negatively charged FITC-BSA molecules translocated along the sample channel and stacked at a distance of ~ 500 μm ahead of the center of nano/microchannel interface, where the focal point of the enriched sample plug was held near the nozzle in order to facilitate the ejection process. It should be pointed out that, the assisting pressures in the simulations and experiments are not on the same order due to the following reasons. First, in the 2D simulation, the third dimension of the nanochannel and microchannel is assumed as the default value of 1 m, while in the experiments, eight nanochannels with the overall width of ~ 2.5 μm and depth of ~ 30 nm and microchannels with both width and depth of 50 μm were integrated into the device. The geometry and size of the nano/micro-network can obviously affect the induced internal pressure at the junction and the resulting bulk

flow rate in the sample microchannel.⁴⁰ Second, the lengths of the sample microchannel in the simulations and experiments are 1 mm and ~ 15 mm, respectively. Therefore, the assisting pressure in the experiment is higher than the simulation. On the other hand, compared with the assisting pressure strategy in a single straight nano/microchannel device³⁶, our dual-channel device requires a lower assisting pressure for stabilizing the

concentrated plug. Specifically, in this work, the additional flow does not pass through the nanochannels which have considerably higher hydraulic resistance. Therefore, the external assisting pressure just needs to overcome the relatively lower resistance in the microchannel for the bulk flow enhancement. As a result, the assisting pressure in a dual-channel system is orders of magnitude lower than that in a single channel device.

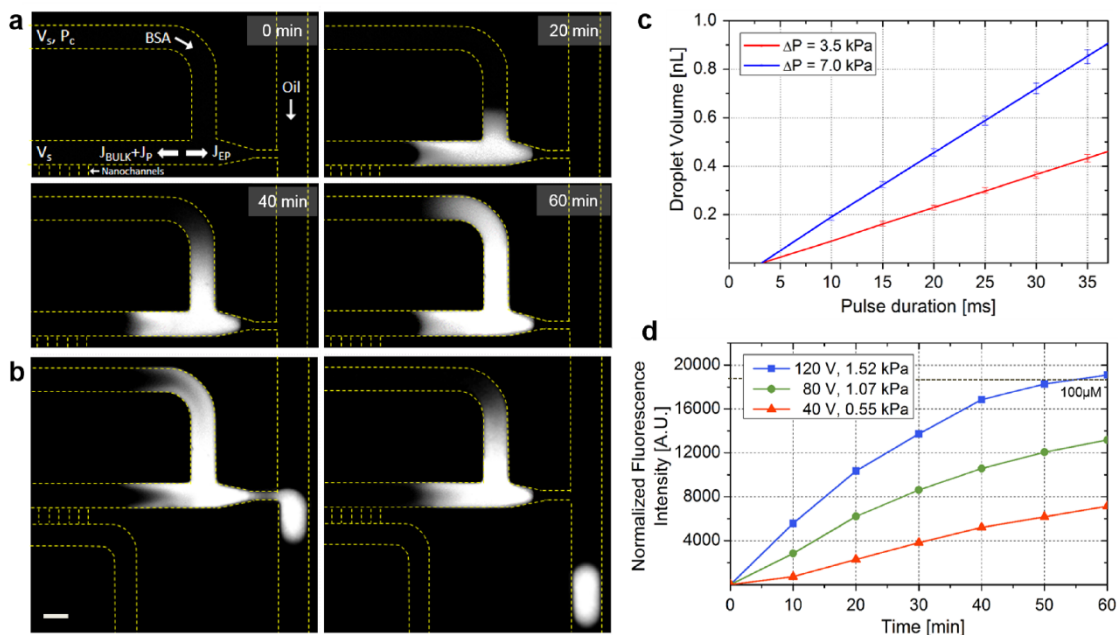


Figure 4. (a) Sequential fluorescence images showing the preconcentration process of FITC-BSA in the nanofluidic concentrator at $V_s = 120$ V and $P_c = 1.52$ kPa for 60 min. (b) Sequential fluorescence images of droplet generation under $\Delta P_i = 3.5$ kPa for 20 ms after the preconcentration. The scale bar is 50 μ m. (c) The droplet volume varies with the amplitude and pulse duration of ΔP_i . (d) Normalized fluorescence intensity variation in the droplets indicates the sample concentration increases with the concentration time for different applying voltages and assisting pressures. The dash line is the reference intensity for 100 μ M FITC-BSA.

On-demand compartmentalization

After the preconcentration process reaches a target concentration, a pressure pulse ΔP_i is applied to the sample channel for droplet ejection. By varying the amplitude and the duration of ΔP_i , the enriched sample plug is encapsulated into a droplet of target volume, as demonstrated in Figure 4(b). In our previous work²³, we have performed a parametric characterization of the droplet size of the DOD system. To calculate the droplet volume, the droplet was treated as a cylinder with two hemispheric ends.⁴¹ As shown in Figure 4(c), the droplet volume increases linearly with the amplitude and pulse duration of ΔP_i , respectively. Therefore, the droplet size can be tuned by varying either the amplitude or the duration of the pressure pulse. The stability and uniformity of the droplet size were also experimentally quantified and validated.²³

We varied the applied voltage V_s as 40 V, 80 V, 120 V, and the concentration time as 10 min, 20 min, 30 min, 40 min, 50 min, and 60 min, respectively. A pressure pulse of 3.5 kPa in amplitude and 20 ms in duration was applied to the sample channel. The concentrated FITC-BSA molecules were encapsulated into water-in-oil droplets of 0.22 nL. Within the droplet, the sample molecules became uniformly distributed after flowing through a mixing channel. The background-subtracted normalized fluorescence intensity values of the generated droplets were used to determine the concentration factors. As shown in Figure 4(d), the concentration factor increased with

accumulation time and the applied voltage. Initially, the peak concentration of the trapped sample molecules increased linearly with time. However, when the concentration reached a high level, the trapping process slowed down due to the nonnegligible diffusion flow.⁴² When the electric potential V_s is increased, both the electrophoretic and electroosmotic flux are enhanced, resulting in the accelerated formation of the depletion zone and delivery of sample molecules. As a consequence, the preconcentration efficiency was improved with an enhanced applied voltage. Even though a higher electric potential could generate a faster concentration rate, in the experiment, the electric potential was limited to 120 V to avoid side effects such as Joule heating⁴³ and electrokinetics instability^{44, 45}. Here, the device was able to achieve 10^4 -fold concentration factor within 60 min.

By utilizing the on-demand compartmentalization of droplets, our new design of a nanofluidic concentrator possesses several inherent merits: (1) long-term stability. The enriched analyte with desired concentration is confined in isolated droplets where diffusion and/or dispersion are fully restricted. (2) High controllability. The sample concentration and volume in a droplet can be precisely tuned by the applied voltage, accumulation time, and pressure pulse, respectively. (3) Readily integration. By coupling mature techniques in droplet-based microfluidics such as merging⁴⁶ and trapping⁴⁷, the concentrator can be easily applied for sequential reaction or detection on-chip or off-chip.

Although the ethanol-induced cracking method for nanoslits fabrication used here are simple and cheap, and can greatly reduce the clogging and aging problems existing in nanomembranes, the number of nanoslits resulted in one substrate is limited, and thus restricts the efficiency of the nanoconcentrator. Further studies can be carried out using nanochannels with higher-density to improve the concentration efficiency such as the nanogrooves manufactured by laser on a PS surface⁴⁸. Besides, the typical sample preconcentration strategies by ICP require the sample molecules to be labeled with fluorescence dyes, which imposes limitation on detection and analysis of unknown samples. Direct electric current or impedance measurement^{49, 50} may be promising for unlabeled samples, e.g., a feedback loop using micro-electrodes embedded near the injection nozzle can be applied to monitor the real-time concentration of the target molecules.

Conclusions

To summarize, we developed a novel droplet-based on-demand preconcentration system that allows for efficient and stable sample enrichment. By ingeniously utilizing the lithography-free nanocracking on the PS surface and a DOD system, our on-demand nanofluidic concentrator can achieve a 10⁴-fold concentration enrichment in encapsulated droplets and reconcile the limitations of sample diffusion and dispersion in conventional concentrators. We also proposed a novel assisting pressure strategy for sample plug stabilization and localization. By investigating the mechanism in two-dimensional numerical simulations, we revealed the complicated interaction among electrophoretic and electroosmotic migration as well as the pressure induced motion during the preconcentration process in the nano/microchannel network. Through proper tuning the assisting pressure, the preconcentrated sample plug was positioned at the ejection nozzle and then encapsulated into a size-controllable water-in-oil droplet. We further demonstrated that the preconcentration factor can be controlled by adjusting the applied voltage and accumulation time. This device can not only dramatically reduce the detection limit of biomarkers, but also allow for facile integrations with other analytical devices for many valuable applications such as enzyme activity assays, protein immunoassays, environmental analysis, etc.

Acknowledgements

This work was supported by the Research Grants Council of Hong Kong under General Research Fund (Grant No. 621113) and the National Science Foundation of China (Grant No. 61006086, 61271161 and 61271162).

Notes and references

^a Bioengineering Graduate Program, Biomedical Engineering Division, The Hong Kong University of Science and Technology, Hong Kong, China. E-mail: meshyao@ust.hk.

^b Department of Mechanical and Aerospace Engineering, The Hong Kong University of Science and Technology, Hong Kong, China.

^c State Key Laboratory of Transducer Technology, Shanghai Institute of Microsystem and Information Technology, Chinese Academy of Sciences, China. E-mail: zhouhb@mail.sim.ac.cn

† Electronic Supplementary Information (ESI) available: Detailed fabrication and alignment, experimental setup, and fluorescence intensity calibration. See DOI: 10.1039/b000000x/

1. K. Strimbu and J. A. Tavel, *Current opinion in HIV and AIDS*, 2010, **5**, 463.
2. D. Barh, A. Carpi, M. Verma and M. Gunduz, *Cancer Biomarkers: Minimal and Noninvasive Early Diagnosis and Prognosis*, CRC Press, 2014.
3. M. C. Breadmore, A. I. Shallan, H. R. Rabanes, D. Gstoettenmayr, A. S. Abdul Keyon, A. Gaspar, M. Dawod and J. P. Quirino, *Electrophoresis*, 2013, **34**, 29-54.
4. D. M. Osbourn, D. J. Weiss and C. E. Lunte, *Electrophoresis*, 2000, **21**, 2768.
5. B. Jung, R. Bharadwaj and J. G. Santiago, *Electrophoresis*, 2003, **24**, 3476-3483.
6. B. Jung, R. Bharadwaj and J. G. Santiago, *Analytical Chemistry*, 2006, **78**, 2319-2327.
7. R. K. Perdue, D. R. Laws, D. Hlushkou, U. Tallarek and R. M. Crooks, *Analytical chemistry*, 2009, **81**, 10149-10155.
8. Y.-C. Wang, A. L. Stevens and J. Han, *Analytical Chemistry*, 2005, **77**, 4293-4299.
9. L. F. Cheow and J. Han, *Analytical chemistry*, 2011, **83**, 7086-7093.
10. M. Shen, H. Yang, V. Sivagnanam and M. Gijs, *Analytical chemistry*, 2010, **82**, 9989-9997.
11. A. Mani, T. A. Zangle and J. G. Santiago, *Langmuir*, 2009, **25**, 3898-3908.
12. S. M. Kim, M. A. Burns and E. F. Hasselbrink, *Analytical Chemistry*, 2006, **78**, 4779-4785.
13. A. Plecis, C. m. Nanteuil, A.-M. Haghiri-Gosnet and Y. Chen, *Analytical Chemistry*, 2008, **80**, 9542-9550.
14. S. H. Ko, Y.-A. Song, S. J. Kim, M. Kim, J. Han and K. H. Kang, *Lab on a Chip*, 2012, **12**, 4472-4482.
15. L.-H. Yeh, M. Zhang, S. Qian, J.-P. Hsu and S. Tseng, *The Journal of Physical Chemistry C*, 2012, **116**, 8672-8677.
16. H. Chun, T. D. Chung and J. M. Ramsey, *Analytical chemistry*, 2010, **82**, 6287-6292.
17. Z. Wang, T. Han, T.-J. Jeon, S. Park and S. M. Kim, *Sensors and Actuators B: Chemical*, 2013, **178**, 683-688.
18. J. Quist, S. J. Trietsch, P. Vulto and T. Hankemeier, *Lab on a Chip*, 2013, **13**, 4810-4815.
19. X. Niu, B. Zhang, R. Marszalek, O. Ces, J. Edel and D. Klug, *Chem. Commun.*, 2009, 6159-6161.
20. Y. Zhao, F. Pereira, H. Morgan and X. Niu, *Lab on a Chip*, 2014, **14**, 555-561.
21. X. Huang, W. Hui, C. Hao, W. Yue, M. Yang, Y. Cui and Z. Wang, *Small*, 2014, **10**, 758-765.
22. C.-H. Chen, A. Sarkar, Y.-A. Song, M. A. Miller, S. J. Kim, L. G. Griffith, D. A. Lauffenburger and J. Han, *Journal of the American Chemical Society*, 2011, **133**, 10368-10371.
23. H. Zhou and S. Yao, *Microfluidics and Nanofluidics*, 2014, **16**, 667-675.
24. H. Zhou, G. Li and S. Yao, *Lab on a Chip*, 2014, **14**, 1917-1922.
25. C. N. Baroud, F. Gallaire and R. Dangla, *Lab on a Chip*, 2010, **10**, 2032-2045.

26. B.-Y. Xu, J.-J. Xu, X.-H. Xia and H.-Y. Chen, *Lab on a Chip*, 2010, **10**, 2894-2901.
27. V. Sunkara, D.-K. Park, H. Hwang, R. Chantiwas, S. A. Soper and Y.-K. Cho, *Lab on a Chip*, 2011, **11**, 962-965.
28. X. Jin, S. Joseph, E. N. Gatimu, P. W. Bohn and N. Aluru, *Langmuir*, 2007, **23**, 13209-13222.
29. M. Jia and T. Kim, *Analytical chemistry*, 2014, **86**, 7360-7367.
30. U. Böhme and U. Scheler, *Chemical Physics Letters*, 2007, **435**, 342-345.
31. H. Daiguji, *Chemical Society Reviews*, 2010, **39**, 901-911.
32. R. B. Schoch, J. Han and P. Renaud, *Reviews of Modern Physics*, 2008, **80**, 839.
33. T. A. Zangle, A. Mani and J. G. Santiago, *Chemical Society Reviews*, 2010, **39**, 1014-1035.
34. G.-p. KONG, X. ZHENG, Z.-h. SILBER-LI and Z. XU, *Journal of Hydrodynamics, Ser. B*, 2013, **25**, 274-279.
35. Y. S. Choi and S. J. Kim, *Journal of colloid and interface science*, 2009, **333**, 672-678.
36. A.-C. Louër, A. Plecis, A. Pallandre, J.-C. Galas, A. Estevez-Torres and A.-M. Haghiri-Gosnet, *Analytical Chemistry*, 2013, **85**, 7948-7956.
37. R. T. Kelly and A. T. Woolley, *Journal of separation science*, 2005, **28**, 1985-1993.
38. K.-B. Sung, K.-P. Liao, Y.-L. Liu and W.-C. Tian, *Microfluidics and Nanofluidics*, 2013, **14**, 645-655.
39. S. J. Kim, Y.-C. Wang, J. H. Lee, H. Jang and J. Han, *Physical review letters*, 2007, **99**, 044501.
40. K.-D. Huang and R.-J. Yang, *Microfluidics and nanofluidics*, 2008, **5**, 631-638.
41. A. Bransky, N. Korin, M. Khoury and S. Levenberg, *Lab Chip*, 2009, **9**, 516-520.
42. A. Rohani, W. Varhue, Y.-H. Su and N. S. Swami, *Biomicrofluidics*, 2014, **8**, 052009.
43. B. Cetin and D. Li, *Electrophoresis*, 2008, **29**, 994-1005.
44. F. C. Leinweber and U. Tallarek, *The Journal of Physical Chemistry B*, 2005, **109**, 21481-21485.
45. H.-C. Chang, G. Yossifon and E. A. Demekhin, *Annual Review of Fluid Mechanics*, 2012, **44**, 401-426.
46. X. Niu, S. Gulati and J. B. Edel, *Lab on a Chip*, 2008, **8**, 1837-1841.
47. W. Wang, C. Yang and C. M. Li, *Lab on a Chip*, 2009, **9**, 1504-1506.
48. E. Rebollar, I. Frischauf, M. Olbrich, T. Peterbauer, S. Hering, J. Preiner, P. Hinterdorfer, C. Romanin and J. Heitz, *Biomaterials*, 2008, **29**, 1796-1806.
49. M. Varshney, Y. Li, B. Srinivasan and S. Tung, *Sensors and Actuators B: Chemical*, 2007, **128**, 99-107.
50. P.-S. Chung, Y.-J. Fan, H.-J. Sheen and W.-C. Tian, *Lab on a Chip*, 2015, **15**, 319-330.